The Borderless World of Chemical Bonding Across the Van der Waals Crust

Jorge Echeverría,[a] Santiago Alvarez[b]

Supporting Information

Methods

The QTAIM analysis of the electron density to generate Figure 1d was done on the DFT wavefunction from a B3LYP/def2-TZVP optimization of the Cl_2 molecule by means of AIMAll.[1] For the energy decomposition analysis (EDA) we used the second-generation ALMO-EDA method[2] implemented in Q-Chem 5.3.[3] The ALMO-EDA scheme decomposes the interaction energy between two fragments into terms that are chemically meaningful $\Delta E_{int} = \Delta E_{FRZ} + \Delta E_{POL} + \Delta E_{CT}$, where ΔE_{FRZ} can be further decomposed into ΔE_{ELEC}, ΔE_{PAULI} and ΔE_{DISP}. All EDA calculations were carried out at the M06-2X/def2-TZVPD level of theory. The effect of the addition of Grimme's D3 dispersion correction[4] was tested for the case of the Ar_2 dimer (see Table S4), and found to enhance the dispersion term (and, consequently, the interaction energy) by less than 0.04 kcal/mol for penetrations as low as -40%, becoming significant only at very low penetrations (i.e., distances longer than 4.6 Å).

Structural searches were carried out in one or more of the CSD, ICSD and MOGADOC databases, depending on the systems studied in each case. Structural data for layered solids were retrieved from the ICSD by searching for the following structural types: graphite, CdI_2, $CdCl_2$, NbS_2, MoS_2, WTe_2, $TaSe_2$, $RhBr_3$, BiI_3, and NbS_3. The X···X intramolecular contacts between *gem* atoms in AX_n compounds (A = element of groups 14, 15 or 16; X = H or halogen) were obtained from gas phase data in the MOGADOC database, except for A = Sn and X = Br or I, obtained from the CSD structures of $MeSnBr_3$ and $MeSnI_3$, respectively (refcodes yizzow and genxig). Data for H···H *gem* contacts in sp^2-CH_2 groups were obtained as averages of 8 CSD structural data for ethylene. Table S15. In the CSD searches disordered structures were disregarded, except for a few cases for which too little information could be obtained with such a restriction. In general, only structures with R ≤ 7.5% were searched for, and the criterion was made more stringent for those searches for which there is a large (R ≤ 5.0%: agostic contacts, R_3N-H···X hydrogen bonds) or very large (R ≤ 2.5%, as for all O-H···X hydrogen bonds) number of structures available. On the contrary, the restriction was released to R ≤ 10% for cases for which a too small number of structures would result, as for the [1.1.1]bicyclopentanes. For the study of the η^5-MCp fragments, double-decker, inverted sandwich and polymeric structures were disregarded, and only structures whose shortest and longest M-C distances differ by at most 0.25 Å were retained. For the agostic interactions in square planar complexes, only angles between the M···C vector and the ML_4 plane of at most 30° were considered.

Appendix A. Volume of the Van der Waals Crust

The volume of the VdW crust of a given atom can be obtained from its Van der Waals and covalent radii:

$$V_{crust} = 4\pi \, (v^3 - r^3)/3$$

The volume of the Van der Waals sphere is $4\pi \cdot r_{VdW}^3/3$, and the portion of that sphere occupied by the Van der Waals crust is given by

$$100*(1- r^3/v^3)$$

Appendix B. Penetration of Misfit Van der Waals Crusts

When two atoms in close proximity have crusts of significantly different widths, the penetration of the widest one into the crust of the thinnest one is higher at a given distance. In case one is interested on the different penetrations of the two atoms, we can define individual penetration measures (see Figure S1), those measures are given by the following expressions.

$$p_A = \frac{v_A + v_B - d_{AB}}{v_A - r_A}$$

$$p_B = \frac{v_A + v_B - d_{AB}}{v_B - r_B}$$

Assuming atom B to be larger than atom A, i.e., $r_A < r_B$, $v_A < v_B$, and $w_A < w_B$, the penetration of the crust of A by B, p_B, is zero when the two VdW spheres are just touching each other (Figure S1a), and becomes 100% when the VdW sphere of B contacts the valence shell of A (Figure S1b), i.e., $d_{AB} = r_A + v_B$. When the Van der Waals sphere of A touches the valence sphere of B, i.e., $d_{AB} = v_A + r_B$, $p_A = 100\%$ (Figure S1c). Finally when the two valence spheres get in touch, $p_{AB} = 100\%$ (Figure S1d). It follows that $p_B > p_A > p_{AB}$ for all distances shorter than the Van der Waals radii sum.
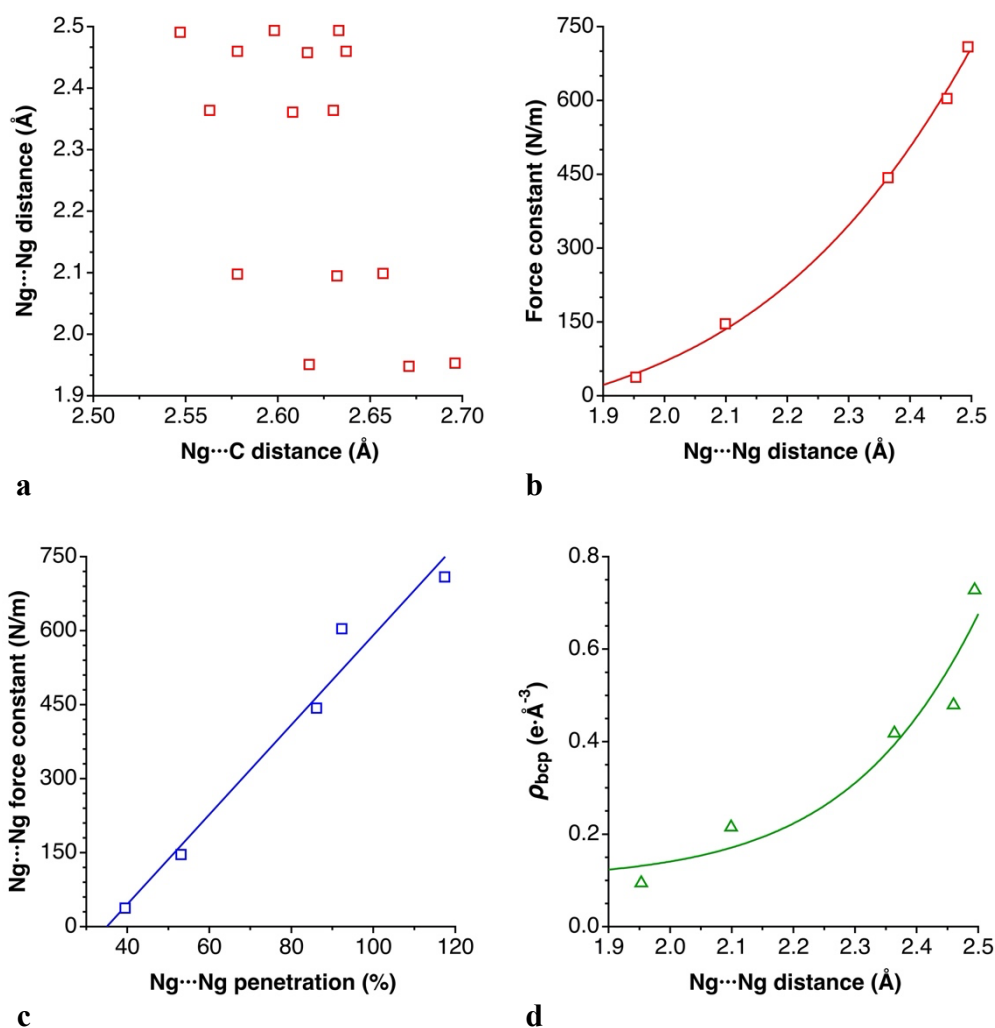
Figures

Figure S1. (**a**) Scatterplot of Ng···Ng and Ng···C distances in $Ng_2@C_{60}$ (Ng = Noble gas). (**b**) Correlation between the force constant and the Ng···Ng bond distance, and (**c**) between the force constant and the Ng···Ng penetration index. (**d**) Relationship between the electron density at the Ng-Ng bond critical point in $Ng_2@C_{60}$ and the Ng···Ng distance. Elaborated from data published by Krapp and Frenking.[5]
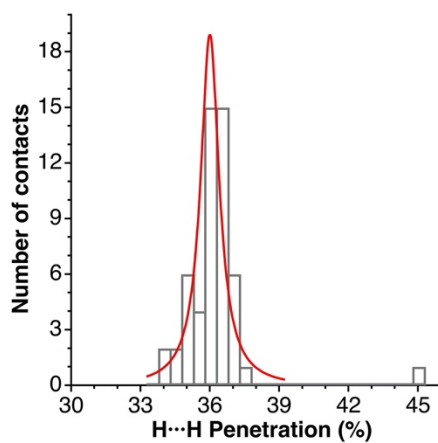

Figure S2. Distribution of H···H contacts in methyl groups in the CSD, and fitting to a Lorentzian function. Only neutron diffraction studies, with R ≤ 2.5%, and no disorder.
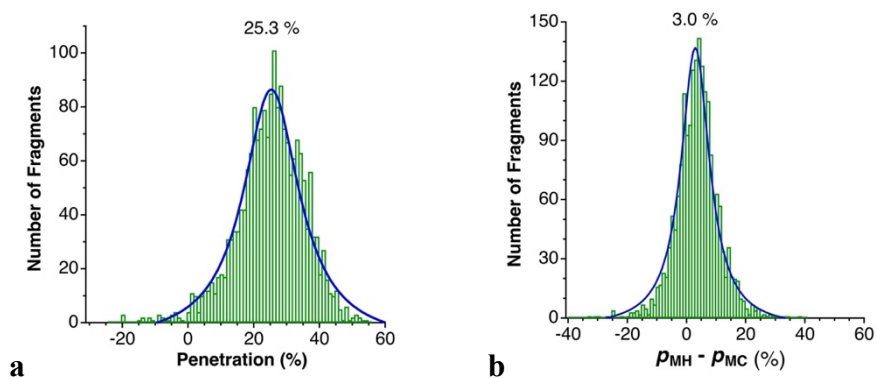
Figure S3. Intramolecular interactions involving C-H bonds and transition metals: distribution of (**a**) M-H penetrations and (**b**) difference between the M-H and M-C penetrations.
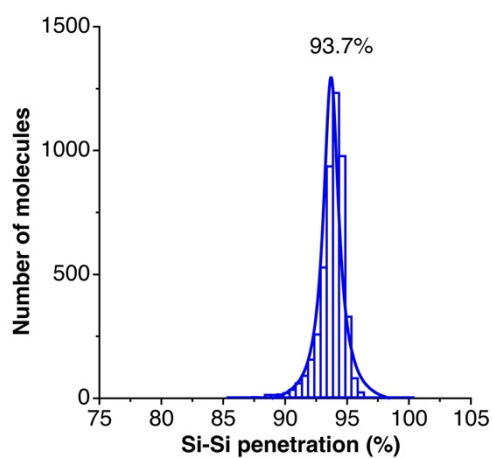

Figure S4. (**a**) Distribution of the Si-Si penetration in sp^3-sp^3 Si-Si single bonds.
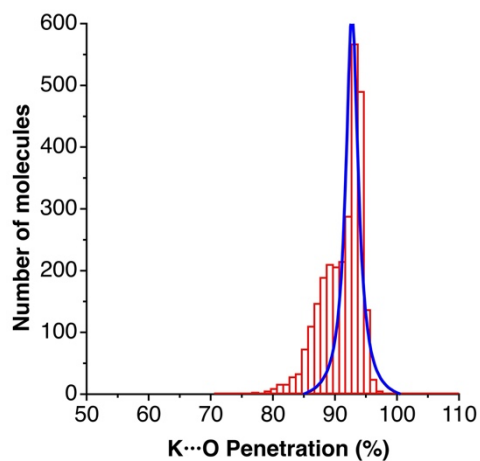

Figure S5. Distribution of K···O penetration indices for contacts between K^+ ions and the 18-crown-6 ether.
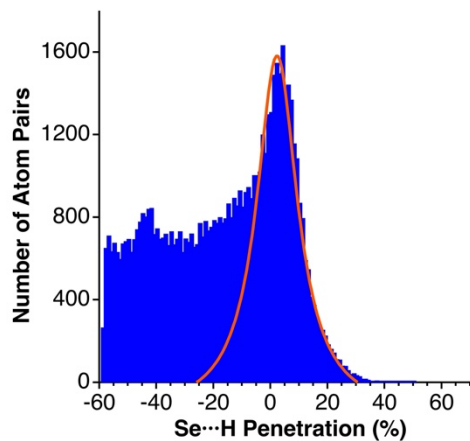
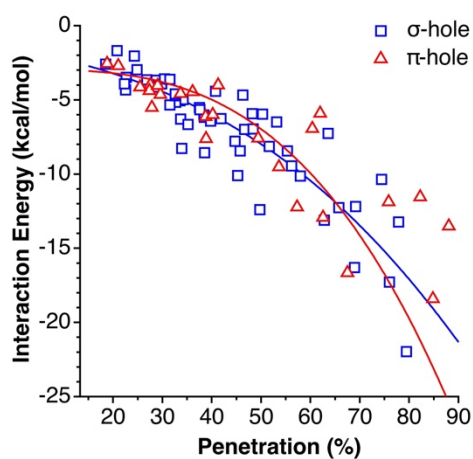**Figure S6**. Distribution of the penetration indices for Se···H contacts in the CSD.

Figure S7. Dependence of the interaction energy on the penetration index for the σ- and π-hole bonded systems calculated by Murray and Politzer.[6]
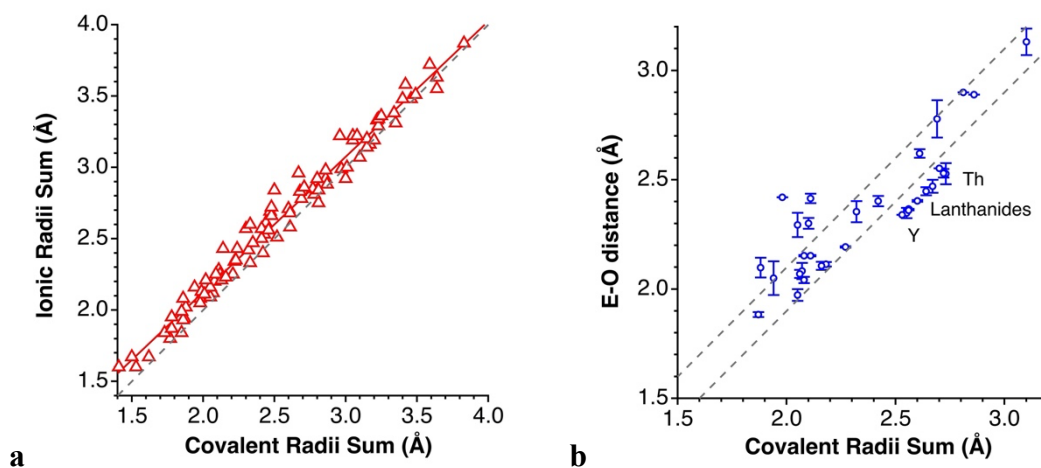

a

b

Figure S8. (a) Comparison of the covalent and ionic radii sums for 92 AX atom pairs, where A is an *s* block element and X a *p* block element. The dashed line represents the ideal case in which the two sums are identical. **(b)** Comparison of the cation-oxygen distances in aqueous solution[7] with the covalent radii sums. The dashed lines indicate a range of ± 0.1 Å from the full coincidence of the two values.
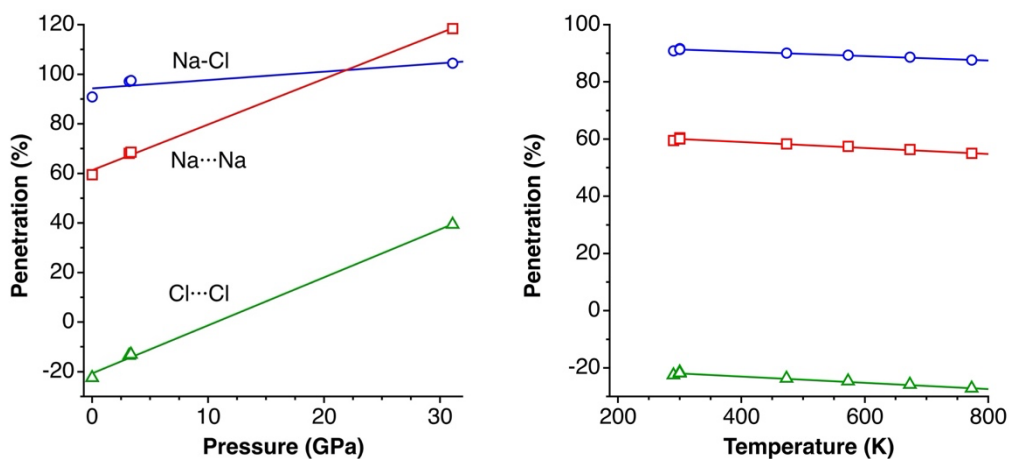
Figure S9. Penetration indices between neighbours in the cubic structure of NaCl as a function of the applied pressure (left) and of the temperature (right).
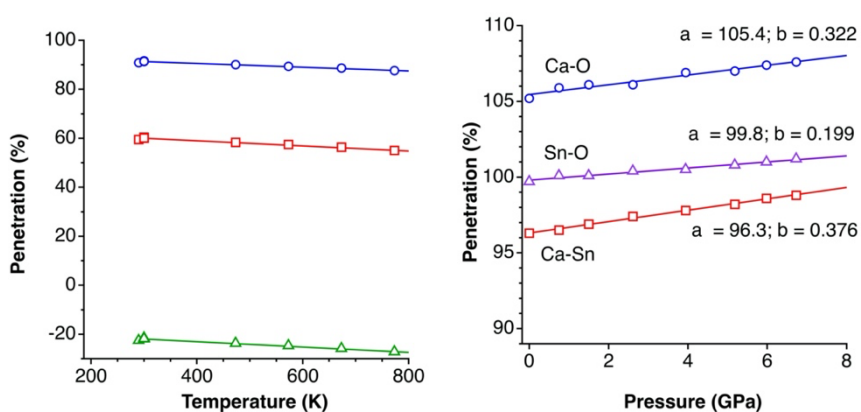

Figure S10. Variation of the penetration indices in the perovskites $CaGeO_3$ with temperature (left) and $CaSnO_3$ with pressure (right) with the least-squares fitting parameters for a linear equation $p_{AB} = a + b \cdot P$.
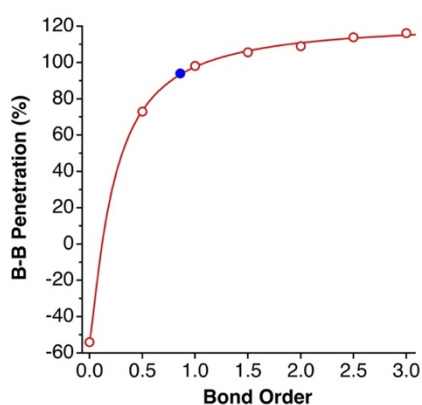

Figure S11. Variation of the average B-B penetration indices found in the CSD for each formal bond orders. The penetration index of compound **9** has been arbitrarily chosen as representative of a non-bonding distance with a 0 bond order. The solid circle corresponds to the penetration in B2H6 interpolated for a bond order of 0.86. The esd's are less than 3% in all cases.
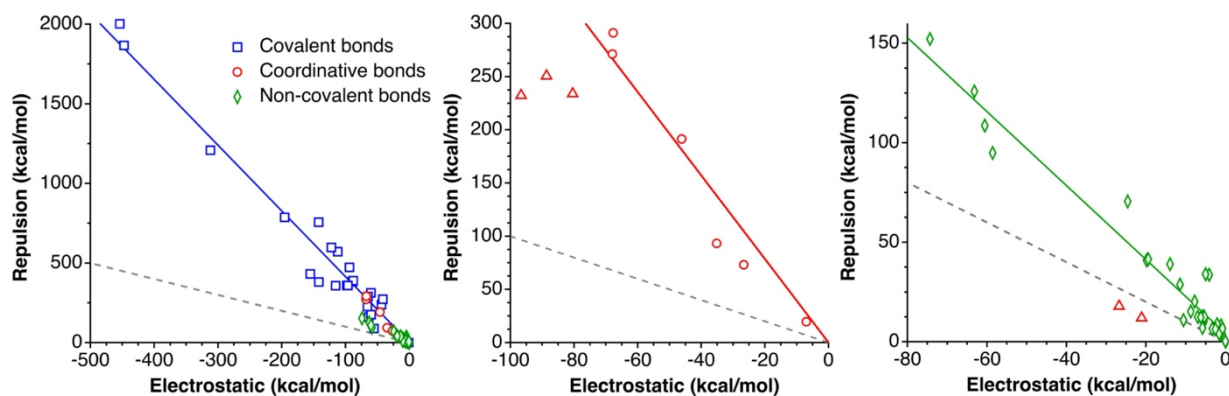
Figure S12. (**a**) Correlation between the Electrostatic and Pauli components of the interaction energies reported by Kumar et al.[8] (**b**) Close-up of the data for coordinative bonds (the outliers shown as triangles correspond to systems with N as a donor atom and B as a Lewis acid). (**c**) Close-up of the data for the non-bonded interactions (the outliers correspond to systems with NH3 or H2O as Lewis bases and LiF as Lewis acids). The dashed lines indicate the borderline that separates systems with a net attractive energy resulting from the electrostatic and Pauli terms (below the line) from those with a net repulsive energy (above the line).
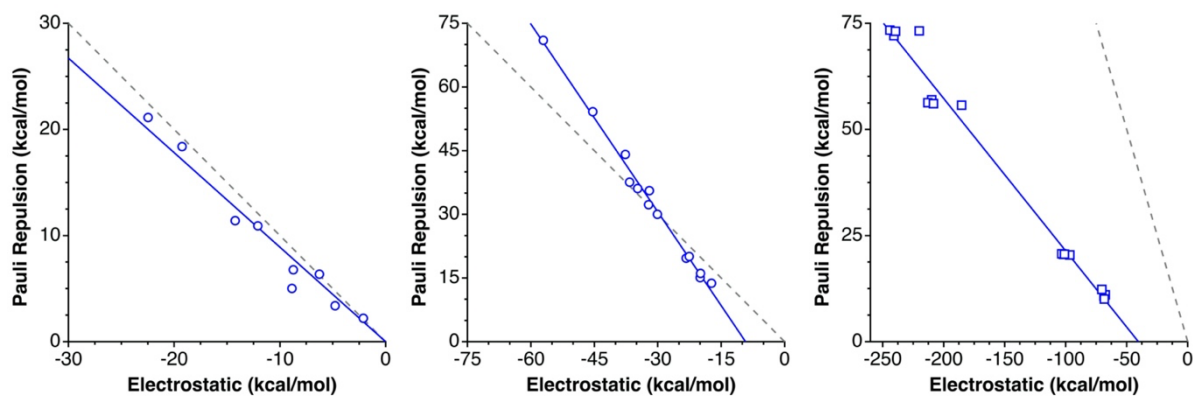

Figure S13. Correlation between the Electrostatic and Pauli components of the interaction energies reported by Grabowski[9] for systems (**a**) with a single hydrogen atom and (**b**) formed by dimers of carboxylic acids, and (**c**) by Madureira et al.[10] for ion pairs.

Tables

Table S1   Covalent and Van der Waals radii, widths of the Van der Waals crust (in Å), and portions of the volume of the Van der Waals sphere occupied by the crust and by the valence sphere (%).

Tables S2-S6. Energy decomposition analysis of the Ng_2 (Ng = He, Ne, Ar, Kr, Xe) adducts at variable distances.

Table S7 - Structural Data for Noble Gas Atom Pairs and for Noble Gases in the Solid State. ID numbers refer to the MOGADOC and ICSD databases for gases and solids, respectively.

Tables S8. Penetrations for bonds and contacts in Ne@p-NC-Ph-OH, at variable applied pressure (Figure 8). Penetration and interaction energies for noble gases enclathrated in cubane, dodecahedrane and buckminsterfullerene (Figure 10).

Tables S9. Penetrations and interaction energies for noble gases in fullerene cages $Ng@C_{60}$ and $Ng_2@C_{60}$ (Figures 11 and S1).

Tables S10. Penetrations and interaction energies for noble gases interacting with XPh molecules (X = halogen, Figure 12).

Tables S11. Largest interlayer penetrations in 2D solids (Figure 14).

Tables S12. Penetration indices for metallophilic contacts of square planar and linear complexes in the CSD (Figure 16).

Tables S13. Penetration indices for secondary interactions between square planar complexes (Rh, Ni, Pd, Pt, Au) and a phenyl group (Figure 17a) obtained from CSD structures.

Tables S14. Penetration indices for secondary interactions between transition metals and an O atom (Figure 17), grouped by periods, obtained fro CSD structures.

Tables S15. Penetration indices for intramolecular contacts between *gem* atoms (Figures 18a-b).

Table S16. Bond angles and intramolecular penetration indices for main group compounds (Figure 18c).

Table S17. Penetrations and bond angles for agostic and σ-bond interactions (Figure 21).

Table S18. OH···X penetration indices for hydrogen bonds (X = O and Cl, Figure 22).

Table S19. Penetration indices for $R_3NH···X$ hydrogen bonds (X = F, Cl, Br, I) found in the CSD (Figure 23).

Table S20. Dissociation energies of hydrogen-bonded complexes comprising H···O, H···N, H···F, H···C and H···H contacts reported by Grabowski and Sokalski, and the corresponding penetration indices (Figure 24). Penetration indices for weak hydrogen bonds C-H···F, C-H···O, C-H···N and C-H···S calculated from structural data in the CSD.

Table S21. F-H penetrations in the F-H-F⁻ anion and O···H penetrations in the $H_2O···H^+···OH_2$ cation. (Figures 25a and c)

Table S22. Penetration indices and binding energy for the X⁻···E hole bonds in adducts **6a** (X = F, Cl, Br; E = Si, Ge, Sn), with binding energies and interatomic distances from Frontera and coworkers[11] (Figure 27a). Data for Figure 27b: Penetration indices and interaction energies of adducts **6b** at their energy minima (distances and interaction energies from refs. [12,13]); of R_3Pn-X^+ ions with NC-A (A = H and Li) **6c**, where X, R = H or F; Z = N, P, As (energies and distancers from ref. [14]); R-EY₃···X⁻ adducts **6d** (data, exept for penetration indices from ref. [13]) and ion pairs

6e (energies and distances from ref. [15]). Data for Figure 27c: Frozen and Orbital interaction energy components calculated by Wang et al.[13] for adducts **6b**, and D-X penetrations calculated in the present work.

Table S23. Penetration indices for several diatomic species with one-, two-, or three- σ-electron bonds in the gas phase. (Figure 28).

Table S24. Penetration indices of Ng-Ng$^+$ half bonds and the deuterium-X and Csp^3-X single bonds on the difference of the Mulliken electronegativity. Data calculated from gas phase and solid state structures (Figure 29). Data for the C-X single bonds (X = halogen) for comparison.

Table S25. Wiberg bond order from ref. [16] and Xe-O penetration indices in the adduct of XeO$_3$ with the crown ether 15-crown-5, covering both the Xe-O bonds (large Xe-O penetration indices) and the Xe$\cdots$O contacts with the five crown oxygens (Figure 31).

Table S26. Average M-H penetration indices and esd's for transition metal complexes with a bridging hydride for different nuclearities. M-M and M-H penetrations in μ_4-H tetrahedral tetranuclear complexes with and without metal-metal bonds. Average M-C penetration indices and esd's for transition metals with terminal and bridging carbonyl ligands of different nuclearities (Figure 32).

Table S27. Penetration indices for the different metal-ligand bonds in semibridging carbonyl complexes. (**b**). (Figure 33a)

Table S28. Difference between the M-C and M-N penetrations in η^2-nitrile (R–C≡N) and isonitrile (R–N≡C) complexes of transition metals (Figure 33b).

Table S29. Penetration indices of the Ng-M bonds in Ng-M-X complexes in the gas phase, where Ng = Ne, Ar, Kr, Xe; M = Cu, Ag, Au, and X = F, Cl, Br, I (Figure 34). Interatomic distances from the MOGADOC database.

Table S30. X$\cdots$N penetration indices and average X$\cdots$N-C angle for silatranes (X = Si), germatranes (X = Ge) and fosfatranes (X = P) (Figure 35).

Table S31. penetration indices between the two apical atoms in trigonal bipyramidal C$_5$ cores **17** and **18** with different framework electron counts (Figure 36).

Table S32. M-C penetration indices and esd's in M(η^5-C$_5$R$_5$) groups, where M is any element of groups 1-16 or a rare earth.. E-C penetration indices and esd's for all elements of the same periodic group in η^6-bonded or weakly interacting E-Benzene fragments and average values and esd's of all the lanthanides (Ln) and actinides (An) η^6-coordinated by benzene and of the intermolecular H$\cdots$Benzene contacts. The data for groups 1, 2, 16, 17, 18 have been retrieved as intermolecular contacts (Figures 38 and 39).

Table S33. Dependence of the Ng-benzene penetration index on the covalent radius of the noble gas (Figure 41).

Table S34. Cation-anion (A-X), cation-cation (A$\cdots$A), and anion-anion (X$\cdots$X) penetration indices in a sample of AX compounds with the NaCl structure (Figure 43a). Penetrations in the perovskite structures as a function of the temperature (CaGeO$_3$) and pressure (CaSnO$_3$, Figure S10).

Tables S35-S37. Average penetration indices and esd's of several single, double and triple element-element bonds, as deduced from the analysis of crystal structural data from the CSD (Figure 43b).

Table S38. Penetration indices in ethers, CO$_2$, transition metal MO$_2$ and actinyl AnO$_2$ groups (Figure 45a).(**b**) Breakdown of the actinyl peak by element and oxidation state.

Table S39. Breakdown of the actinyl penetration indices by element and oxidation state (Figure 45b).

Table S40. Comparison of the sums of ionic and covalent radii for 122 atom pairs.

REFERENCES
1   AIMAll v. 19.10.12 (Gristmill Software, Overland Park, KS, 2019).
2   Horn, P. R., Mao, Y. & Head-Gordon, M. Probing non-covalent interactions with a second generation energy decomposition analysis using absolutely localized molecular orbitals. . *Phys. Chem. Chem. Phys.* **18**, 23067-23079 (2016).
3   Epifanovsky, E. *et al.* Software for the frontiers of quantum chemistry: An overview of developments in the Q-Chem 5 package. *J. Chem. Phys.* **155**, 084801 (2021).
4   Grimme, S., Antony, J., Ehrlich, S. & Krieg, H. A consistent and accurate ab initio parametrization of density functional dispersion correction (DFT-D) for the 94 elements H-Pu. *J. Chem. Phys.* **132**, 154104 (2010).
5   Krapp, A. & Frenking, G. Is This a Chemical Bond? A Theoretical Study of Ng_2@C_{60} (Ng=He, Ne, Ar, Kr, Xe). *Chem. Eur. J.* **13**, 8256-8270 (2007).
6   Murray, J. S. & Politzer, P. Interaction and Polarization Energy Relationships in σ-Hole and π-Hole Bonding. *Crystals* **10**, 76 (16 pages) (2020).
7   Marcus, Y. Ionic Radii in Aqueous Solutions. *Chem. Rev.* **88**, 1475-1498 (1988).
8   Kumar, N., Saha, S. & Sastry, G. N. Towards developing a criterion to characterize non-covalent bonds: a quantum mechanical study. *Phys. Chem. Chem. Phys.* **23**, 8478-8488 (2021).
9   Grabowski, S. J. What Is the Covalency of Hydrogen Bonding? *Chem. Rev.* **111**, 2597-2625 (2011).
10   Madureira, L. M. P., Dias, L. G., Parreira, R. L. T. & Caramori, G. F. Shedding light on the physical nature of ion pair involving carba-closo-dodecaborate anions. Insights from computation. *Phys. Chem. Chem. Phys.* **25**, 5710-5717 (2023).
11   Bauzà, A., Mooibroek, T. J. & Frontera, A. Tetrel-Bonding Interaction: Rediscovered Supramolecular Force? *Angew. Chem. Int. Ed.* **52**, 12317-12321 (2013).
12   Mo, Y., Danovich, D. & Shaik, S. The roles of charge transfer and polarization in non-covalent interactions: a perspective from ab initio valence bond methods. *J. Mol. Model.* **28**, 274 (2022).
13   Wang, C., Danovich, D., Mo, Y. & Shaik, S. On The Nature of the Halogen Bond. *J. Chem. Theor. Comput.* **10**, 3726-3737 (2014).
14   Grabowski, S. J. Pnicogen and tetrel bonds—tetrahedral Lewis acid centres. *Struct. Chem.* **30**, 1141-1152 (2019).
15   Bartashevich, E., Matveychuk, Y. & Tsirelson, V. Identification of the Tetrel Bonds between Halide Anions and Carbon Atom of Methyl Groups Using Electronic Criterion. *Molecules* **24**, 1083 (1012 pages) (2019).
16   Marczenko, K. M., Mercier, H. P. A. & Schrobilgen, G. J. A Stable Crown Ether Complex with a Noble-Gas Compound. *Angew. Chem. Int. Ed.* **57**, 12448-12452 (2018).